AGU PUBLICATIONS

JGR

Journal of Geophysical Research: Space Physics

RESEARCH ARTICLE
10.1002/2017JA024224

Storm and Substorm Causes and Effects at Midlatitude Location for the St. Patrick's 2013 and 2015 Events

A. Guerrero[1], J. Palacios[1], M. Rodríguez-Bouza[2], I. Rodríguez-Bilbao[2], A. Aran[3], C. Cid[1], M. Herraiz[2,4], E. Saiz[1], G. Rodríguez-Caderot[2,5], and Y. Cerrato[1]

[1]Departamento de Física y Matemáticas, Universidad de Alcalá (UAH), Alcalá de Henares, Spain, [2]Departamento de Física de la Tierra, Astronomía y Astrofísica I (Geofísica y Meteorología), Universidad Complutense de Madrid (UCM), Madrid, Spain, [3]Department de Física Quàntica i Astrofísica i Institut de Ciències del Cosmos, Universitat de Barcelona, Barcelona, Spain, [4]Instituto de Geociencias (UCM,CSIC), Madrid, Spain, [5]Instituto de Matemática Interdisciplinar (UCM), Madrid, Spain

Key Points:
- We decouple storm and substorm effects for midlatitude location during St. Patrick's events
- Substorm effects during storm time at midlatitudes are relevant for space weather hazards
- Comparison of interplanetary features for both events reveals that merging reinforces geoeffectiveness

Correspondence to:
A. Guerrero,
aguerrero@uah.es

Citation:
Guerrero, A., Palacios, J., Rodríguez-Bouza, M., Rodríguez-Bilbao, I., Aran, A., Cid, C., … Cerrato, Y. (2017). Storm and substorm causes and effects at midlatitude location for the St. Patrick's 2013 and 2015 events. *Journal of Geophysical Research: Space Physics*, *122*. https://doi.org/10.1002/2017JA024224

Received 12 APR 2017
Accepted 3 SEP 2017
Accepted article online 11 SEP 2017

Abstract Midlatitude locations are unique regions exposed to both geomagnetic storm and substorm effects, which may be superposed on specific events imposing an extra handicap for the analysis and identification of the sources and triggers. We study space weather effects at the midlatitude location of the Iberian Peninsula for the St. Patrick's day events in 2013 and 2015. We have been able to identify and separate storm and substorm effects on ground magnetometer data from *San Pablo-Toledo* observatory during storm time revealing important contributions of the Substorm Current Wedge on both events. The analysis of these substorm local signatures have shown to be related to the production of effective geomagnetically induced currents and ionospheric disturbances as measured from Global Navigation Satellite Systems data at MAD2 IGS permanent station and not directly related to the storm main phase. The whole Sun-to-Earth chain has been analyzed in order to identify the solar and interplanetary triggers. In both events a high-speed stream (HSS) and a coronal mass ejections (CME) are involved, though for 2015 event, the HSS has merged with the CME, increasing the storm geoeffectiveness. The enhancement of substorm geoeffectiveness is justified by the effects of the inclined magnetic axes of the Sun and of the Earth during equinox period.

1. Introduction

Major processes that take place during geomagnetic storms in the coupled magnetosphere-ionosphere-thermosphere system are generally known, although a number of significant aspects of these responses remain challenging. It is well known that strong localized geospace disturbances occur frequently, threatening our technology, leaving no privileged latitude or longitude position to stay aside of the problem, but the position on the globe where they occur as well as the intensity and the exact time-of-occurrence still scape from successful modeling and/or forecasting. Consequently, individual studies of local geospace responses provide a fundamental tool for space weather research.

St. Patrick's day (17 March) geomagnetic storms in 2013 (hereinafter E13) and 2015 (hereinafter E15) have been extensively analyzed (see, e.g., Gkioulidou et al., 2014; Kataoka et al., 2015; Singh et al., 2015), and also by the works in the special issue *Geospace system responses to the St. Patrick's Day storms in 2013 and 2015* of the *Journal of Geophysical Research: Space Physics*, which are mostly focused on the ionospheric disturbances during the events, as well as Carter, Yizengaw, Pradipta, Retterer, et al. (2016), Nayak et al. (2016), and Piersanti et al. (2017). An evaluation of geomagnetically induced currents (GICs) has been done for 2015 event by Carter, Yizengaw, Pradipta, Weygand, et al. (2016). The severity of the storm according to *Dst* or *SYM-H* peak values has been described, for example, by Cherniak et al. (2015) and Jacobsen and Andalsvik (2016).

In this work we have addressed a comparative analysis concerning the local midlatitude disturbances of the geomagnetic field and ionosphere (as detected by ground stations from the central region of the Iberian Peninsula) without leaving the global picture of the whole Sun-to-Earth chain or the global response on the ground. The sequence of events and the special configuration of the whole system has been analyzed in order to identify global storm variables pertaining to the current understanding of the solar-terrestrial environment, and to be able to isolate the substorm local responses. This procedure allows us to identify hazards that have

been previously underrated, especially for midlatitude locations and mostly because of the still unknown role of the storm-substorm relationship.

At midlatitude locations, the ring current is considered as the greatest contribution to the disturbance magnetic field measured on the ground during the time of a geomagnetic storm. A good indicator of this disturbance is the 1 h resolution *Dst* index (Sugiura, 1965; Sugiura et al., 1991). This index has demonstrated to be the geomagnetic index that most closely represents the system of currents for which it was designed: the ring current energy content (Dessler & Parker, 1959). However, several studies have suggested that the *Dst* index contains contributions from many other sources than the azimuthally symmetric ring current (Alexeev et al., 2001; Arykov & Maltsev, 1993; Campbell, 1973; Dremukhina et al., 1999; Kalegaev & Makarenkov, 2008; Liemohn, 2003; Mayaud, 1980; Ohtani et al., 2001; Tsyganenko & Sitnov, 2005). Moreover, these global geomagnetic indices are not recommended when analyzing local disturbances and other tools are needed for the analysis (Cid et al., 2015; Mayaud, 1980; Saiz et al., 2016). Consequently, in this work we mainly use the horizontal component of the geomagnetic field as the main indicator to infer the source contributions to ground disturbances.

We also pay attention to the midlatitude ionosphere, which is defined as the region that is not affected by subauroral or equatorial phenomena during geomagnetic quiet conditions (Prölss, 2008). This region of the ionosphere, usually considered as the least variable zone, is in fact characterized by the occurrence of numerous signatures such as the recurrent medium scale traveling ionospheric disturbances (MSTIDs) with their own climatology (Tsugawa et al., 2007; Wautelet & Warnant, 2014), or field-aligned irregularities (FAIs) that may appear superposed to MSTIDs (Sun et al., 2015; Wautelet & Warnant, 2015). Under the influence of a geomagnetic storm, the ionospheric total electron content (TEC) may experience modifications with respect to the level of quiet conditions at midlatitudes by a factor ranging from 3 to 10 (Kintner et al., 2008). These variations, called ionospheric storms, are due to the expansion of the equatorial ionospheric anomaly (EIA) to geomagnetic latitudes of 30° (Heelis, 2008; Tsurutani et al., 2004) in which Southern Europe is located. Also, complex plasma transport and electric interactions that model the ionosphere at auroral and subauroral latitudes may also extend their influence to lower latitudinal regions causing storm-enhanced plasma density (SED) regions at high latitudes, and electron density enhancements at near dusk midlatitudes (Foster & Rideout, 2005). Additionally, other kind of perturbations related to the prompt penetration of the electric fields (Foster & Rich, 1998), the equatorward/poleward propagation of large scale traveling ionospheric disturbances (LSTIDs) (Borries et al., 2009; Habarulema et al., 2016) and the extension from high to low latitude of FAIs may also occur during geomagnetic storms (Sun et al., 2015).

In this work, we analyze the sequence of events from the Sun to the Earth that resulted in strong local geospace responses in order to highlight their space weather effects. The data sets used are described in section 2 as well as the processing techniques needed to analyze the local geospace responses at the Iberian Peninsula (∼40°N). Methodology and results are developed in two sections: an analysis of the geospace response in section 3 and the analysis of their solar and interplanetary (IP) sources in section 4. Discussion and conclusions are developed in sections 5 and 6, respectively.

2. Data Sets and Processing

The present study considers the whole Sun-to-Earth chain on the time interval that extends from 13 to 20 March for both years under analysis (2013 and 2015) and uses the following data sets:

1. Data regarding the Sun's high chromosphere and low corona from AIA (Lemen et al., 2012) on board SDO (Pesnell et al., 2012). The corresponding dates belong to equinox periods, which are somewhat critical due to SDO eclipse season and the consequent presence of data gaps. Coronal imaging is acquired by LASCO (Brueckner et al., 1995) on board SOHO (Domingo et al., 1995). The dominant magnetic polarity and filament chirality are deduced through SDO/HMI (Scherrer et al., 2012) line-of-sight magnetograms.
2. Interplanetary in situ data are obtained from different instruments on board ACE spacecraft, located upstream of the Earth at the Lagrangian L1 point. Interplanetary magnetic field (IMF) data from ACE/MAG (Smith et al., 1998) and solar wind plasma data (except density, due to data gaps) come from ACE/SWEPAM (McComas et al., 1998), all ACE data with 64 s resolution. Density data have been obtained from Wind/SWE instrument (Ogilvie et al., 1995) with ≈92 s resolution. Energetic particle differential intensities are obtained from ACE/EPAM (Gold et al., 1998) with 5 min resolution. For the analysis of ionic composition we use data from ACE/SWICS (Gloeckler et al., 1998) with 2 h resolution.

3. Energetic particles arriving the near-Earth environment are obtained by measurements of differential intensities from GOES13-EPEAD (Hanser, 2011) with 5 min resolution.
4. Ground geomagnetic response is analyzed both globally and locally; the global analysis using geomagnetic indices *SYM-H* (ring current), *AL*, and *AU* (auroral activity), as extracted from Kyoto World Data Center, and the local analysis for the Iberian Peninsula through 1 min resolution data from San Pablo-Toledo (SPT, Geographic coordinates 39.55°N, 355.65°E) available through the INTERMAGNET database.
5. The ionospheric response is analyzed also locally for the Iberian Peninsula, using 30 s sampling rate RINEX (Receiver Independent Exchange Format) files from MAD2 IGS permanent station (40.43°N, 355.75°E geographic coordinates).

2.1. Geomagnetic Data Processing

For midlatitude locations, the horizontal component of the geomagnetic field measured at ground stations is expected to be the superposition of effects from different sources: the internal geomagnetic field (main field from the outer core of the Earth and fields from the crust) and external sources like ionospheric, field-aligned, magnetopause, magnetotail, and ring currents.

Considering the period of about 1 week for the events analyzed in this work, and the goal of the paper, which is to evaluate all geomagnetic variations that occur during that period, we need only to substract a reference constant value which will represent all larger timescale variations. Consequently, for each event we have chosen a constant value (H_0) given by the average during the quietest night (less disturbed period) observed during March. The period considered for both, E13 and E15, has been from 22:00 UT on 7 March to 02:00 UT on 8 March. This value has been subtracted from the horizontal component of the geomagnetic field measured at SPT and the remaining signal has been called SPT-H.

A commonly used indicator of hazardous geomagnetic disturbances is the rate of change of the geomagnetic field. In this work we have used the 30 min time derivative of the horizontal component (DER-H), which has resulted to be a good proxy for the production of GICs and their corresponding effects on technology (Schrijver & Mitchell, 2013). Therefore, we have also computed DER-H for the two events analyzed in this paper.

2.2. Ionospheric Data Processing

The ionospheric behavior has been studied through the total electron content (TEC), estimated from dual-frequency Global Navigation Satellite Systems (GNSS) data contained in MAD2 station RINEX files. The slant TEC (sTEC) for each satellite pass and the vertical TEC, vTEC, over the station are obtained for each minute through the calibration technique described in Ciraolo et al. (2007) using an elevation cutoff of 10°. To reduce geometric effects on sTEC an ionospheric thin shell model (Schaer et al., 1996) at an altitude of 350 km is used to convert sTEC into equivalent vTEC (vTECeq) at the ionospheric pierce point (IPP, the point where the line of sight between the satellite and the ground receiver intersects the considered ionospheric layer). This calibration technique is widely used in ionospheric studies as in Zhang et al. (2009), Nigussie et al. (2012), and Asmare et al. (2014).

The relative variation of vTEC (vTECrel) has been used to analyze vTEC variations over MAD2 station. This parameter is defined as the expression in equation (1) and represents deviations with respect to vTEC quiet diurnal variations.

$$\mathrm{vTECrel}_i(\%) = 100 \times \frac{\mathrm{vTEC}_i - \overline{\mathrm{vTEC}_i}}{\overline{\mathrm{vTEC}_i}} \tag{1}$$

where vTEC_i represents the observable value at each epoch, $\overline{\mathrm{vTEC}_i}$ the average value of each epoch, and *i* the epoch (considered every 1 min for this study). The average value is calculated with 3 of the 10 International Quiet Days, IQDs, of the respective month considering the days without solar flares effect. A vTEC variation is considered significant when vTECrel exceeds the threshold value of ±50% (naming a positive phase when the variation is over 50% and a negative phase when it is below −50%).

In addition, the rate of change of TEC (ROT) is computed for each full arc by the first time derivative of the vTECeq as given in equation (2), which is suitable for ionospheric irregularities identification at midlatitudes (Wautelet & Warnant, 2014).

$$\mathrm{ROT}_i = \mathrm{vTECeq}_{i+1} - \mathrm{vTECeq}_i \tag{2}$$

where *i* is the epoch (considered every 1 min).

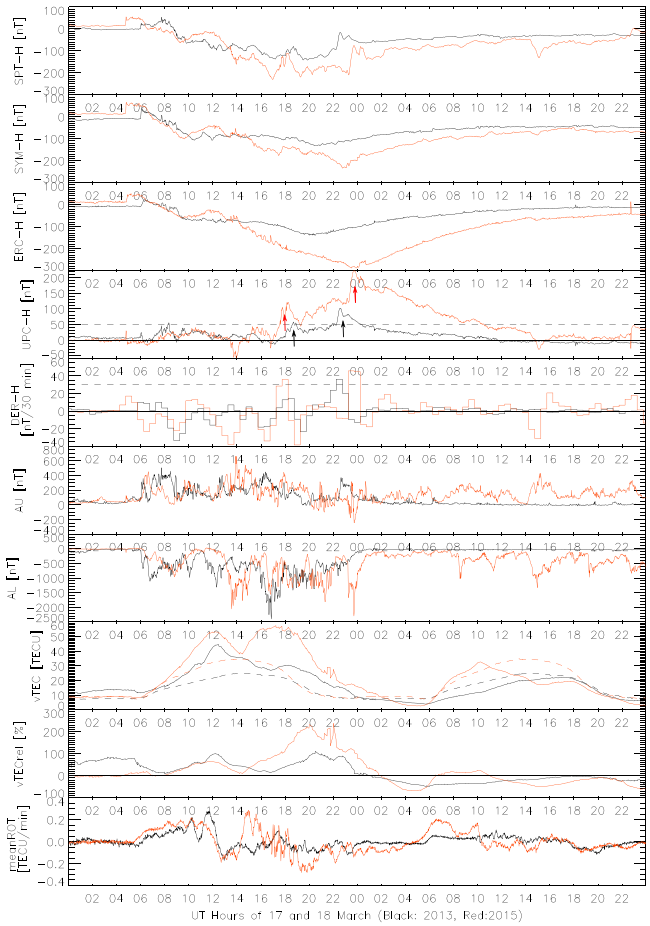

Figure 1. Geospace response for the period 17–18 March 2013 (black) and 2015 (red). From top to bottom: geomagnetic disturbance field at SPT observatory, SPT-H; *SYM-H* geomagnetic index; predicted enhancement of ring current (ERC-H); unpredicted contribution of the horizontal geomagnetic field, UPC-H; derivative of the geomagnetic field, DER-H; geomagnetic index *AU*, geomagnetic index *AL*; vertical total electron content, vTEC; relative variation of TEC, vTECrel, and mean Rate of change of TEC, meanROT. For the signals SPT-H, UPC-H, DER-H, vTEC, vTECrel, and meanROT, MLT is only 16 min time shifted with respect to UT.

In this work, the average of the ROT values (meanROT) in each epoch is used in order to highlight the presence of synchronous ionospheric perturbations in ROT. To reduce the noise related to low-elevation effects such as multipath or the line of sights crossing the low-latitude ionosphere, only the satellites with elevation above 30° have been considered when calculating ROT values at each epoch.

2.3. Expected Ground Magnetic Disturbance From Solar Wind Energy Input

In order to separate local and global disturbances and getting a better distinction between purely magnetospheric effects and those from the solar wind coupling, we have computed the theoretical expected response to solar wind energy input of an azimuthally symmetric ring current (as seen by the horizontal component of the geomagnetic field on the ground). This solar wind-magnetosphere coupling can be analyzed using the well-known empirical relationship given by Burton et al. (1975), reproduced here as equation (3), in which the effect on the horizontal geomagnetic field component due to an enhanced ring current (hereinafter ERC-H$_c$) is described as a system that responds to the input energy function $F(E)$ as a first-order linear time-invariant system with a fixed characteristic time constant (τ).

$$\frac{\mathrm{d}}{\mathrm{d}t}\text{ERC-H}_c = F(E) - \frac{1}{\tau}\text{ERC-H}_c \tag{3}$$

The original formulation given in Burton et al. (1975) yields a value of $\tau = 7.716$ h ($\tau^{-1} = 3.6{\cdot}10^{-5}$ s^{-1}) and a description of the injection function $F(E)$ by the dawn-to-dusk convective electric field ($E_y = VB_z$; where V represents the solar wind speed and B_z stands for the IMF south component in GSM coordinates) as follows:

$$F(E) = \begin{cases} 0 & : \ E_y < 0.50 \ \text{mVm}^{-1} \\ d(E_y - 0.5) & : \ E_y > 0.50 \ \text{mVm}^{-1} \end{cases}$$

where $d = -1.5 \cdot 10^{-3}$ nT mV^{-1} m s^{-1}.

Using equation (3), we obtain ERC-H$_c$ as the convolution of the first-order impulse response and the $F(E)$ signal on the input. ERC-H$_c$ is a prediction of the effects of the ring current enhancement on the horizontal geomagnetic field component due to solar wind energy input; consequently, the prediction (hereinafter ERC-H) has to be delayed to take into account the propagation time from the solar wind measurement position to the ground. We have applied simply the time of propagation at an average solar wind velocity of 600 km s^{-1} for E13 and 500 km s^{-1} for E15 (42 and 50 min, respectively). Furthermore, it is necessary to add the effect of the change of solar wind dynamic pressure and to subtract a *quiet day constant*, as indicated by equation (4).

$$\text{ERC-H} = \text{ERC-H}_c + b(P_d)^{1/2} - c \tag{4}$$

where $b = 0.2$ nT(eV cm^{-3})$^{-1/2}$, $c = 20$ nT as in Burton et al. (1975) and $P_d = N_p V^2 10^{-2}$ eV cm^{-3} with N_p being the solar wind proton density.

We obtain also an unpredicted contribution to the horizontal geomagnetic field (hereinafter UPC-H), in this case for the localization of SPT observatory, as the residual signal that results in subtracting ERC-H from SPT-H. Before subtracting both signals, SPT-H is corrected for the projection of the equatorial ring current at the latitude of SPT station, thus multiplying SPT-H by the cosine of the latitude. The residual UPC-H signal is influenced by all nonsymmetrical current effects as well as local disturbances at midlatitudes like ionospheric, partial ring current or FACs. Both ERC-H and UPC-H are used in this work for the analysis of the geomagnetic response.

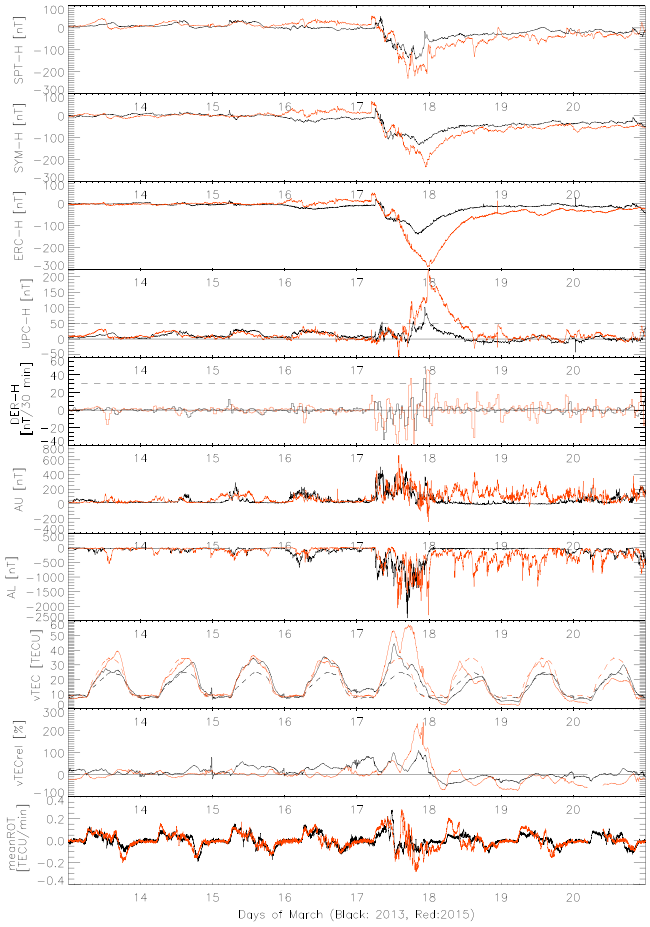

Figure 2. Geospace response for the period 13–20 March 2013 (black) and 2015 (red). From top to bottom, geomagnetic disturbance field at SPT observatory, SPT-H; *SYM-H* geomagnetic index; predicted enhancement of ring current (ERC-H); unpredicted contribution of the horizontal geomagnetic field, UPC-H; derivative of the geomagnetic field, DER-H; geomagnetic index *AU*, geomagnetic index *AL*; vertical total electron content, vTEC; relative variation of TEC, vTECrel, and mean Rate of change of TEC, meanROT.

3. Analysis of Local Geospace Response

The local geospace response has been divided into two sections. In section 3.1 we focus the attention on the days of the storm (i.e., 17–18 March), while in section 3.2 we analyze the background geospace state on a wider time range (before and after the events). In both cases, a comparative analysis has been performed between E13 and E15 for the ground and ionospheric responses. For this purpose, we have arranged the data sets of both events in two overplotted figures: Figure 1 for the period 17–18 March, and Figure 2 for the period 13–20 March (sharing the same panel arrangement).

Each panel in Figures 1 and 2 is an overplot of data series of the events E13 and E15 for which black color is used for E13 and red for E15. The time reference for all data is UT, and no time shifting has been necessary to apply to any of the events (E13 or E15) for their comparison. From top to bottom the figures show the following panels: the horizontal component of the geomagnetic field measured at San Pablo-Toledo observatory with the baseline H_0 removed as described in section 2.1, SPT-H; the *SYM-H* geomagnetic index; the predicted and corrected enhancement of ring current ERC-H as described in section 2.3; the unpredicted contribution of the horizontal geomagnetic field, UPC-H; the derivative of the geomagnetic field, DER-H as described in section 2.1; geomagnetic indices *AU* and *AL*; and the last three panels which show ionospheric parameters vTEC, vTECrel, and meanROT, respectively. On the vTEC panel, a dashed line is overplotted for the quiet vTEC curve used for deriving vTECrel for each event, as described in section 2.2. Notice that SPT observatory and MAD2 station are at 356° geographic longitude; thus, magnetic local time (MLT) is only 16 min time shifted with respect to UT. Therefore, in this study we effectively consider MLT as UT.

3.1. Main Disturbances (17–18 March)

Following Figure 1, the main phases of the geomagnetic storms develop on 17 March from about 5 UT to the end of the day, when the recovery phase starts. The considerably long duration (about 19 h) of the main phase is a common peculiarity for both events. After the main phase, the recovery phase is characterized by high activity in the auroral zone for E15 but low activity for E13, as seen by *AL* and *AU* indices. We can see that most of the features of the main phase, as seen by *SYM-H* index, are well represented by the expected enhanced ring current response to solar wind energy input, described by ERC-H signal. This indicates that even though a long-duration main phase may anticipate a complex scenario, most of their features are explained solely by taking into account the response to solar wind energy input. The expected intensity for E15 is larger than the intensity indicated by *SYM-H* by around 50 nT, pointing out that the strongest storm of the present solar cycle was potentially more intense only, considering solar wind properties. Apart from the difference in the peak intensity of E15, the profile of the expected effects (ERC-H) are well followed by both the geomagnetic index *SYM-H* and the geomagnetic field SPT-H, indicating a strong solar wind-magnetosphere coupling.

Nevertheless, several disturbances are evident in SPT-H that are not present on ERC-H data. They are better seen in their residual signal UPC-H (fourth panel from the top of Figure 1). We have drawn a line at the threshold level of +50 nT as a good value to start considering a geomagnetic disturbance as relevant, similar to the criteria used to classify for moderate geomagnetic storms by *Dst* index (Gonzalez et al., 1994) (this time positive instead of negative).

Two increases in UPC-H data are easily discernible on each of the events, even though less intense for E13. They are seen as double-peaked positive disturbances around dusk and midnight on 17 March. Those four increases have been marked with arrows in Figure 1.

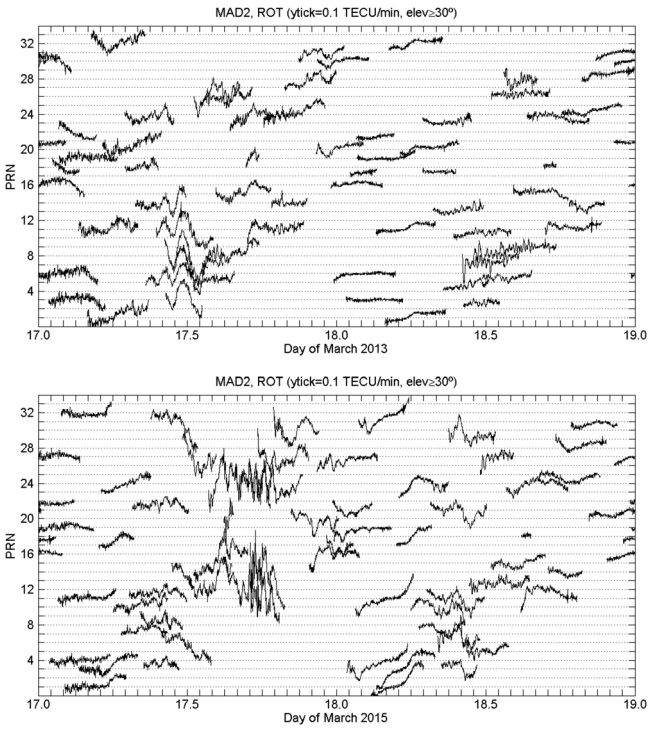

Figure 3. ROT for each GPS satellite over MAD2 station on 17 and 18 March (top) 2013 and (bottom) 2015. Satellites elevation mask: 30°.

At the same timing DER-H shows the highest values, indicating that they are not only intense but also fast changes of the geomagnetic field that can produce GICs and disrupt technology. We have also drawn a line at the threshold level of 30 nT(/30 min), based on the values found by Schrijver and Mitchell (2013); this level is between percentiles 2nd and 5th of the daily maximum values that demonstrated to indicate well the impact of the geomagnetic activity on the U.S. power grid. The three highest increases of UPC-H signal (out of the five commented above) are also followed by DER-H surpassing this threshold level.

The response of the ionosphere as seen by vTEC and its relative variation vTECrel are also similar on both E13 and E15 during 17 March, characterized by two consecutive positive phases (increases over quiet level Prölss, 1995) of ionospheric storm, centered at around 12:00 UT and 18:00 UT, respectively. Disturbances begin at 09:00 UT for E13 and at 08:00 UT for E15; in both cases 3 h after its respective geomagnetic storm sudden commencement (SSC) signature. The maximum value of vTEC observed in the first phase is similar in both events, but in the second phase it is much higher for E15. The peaks of vTEC appear at the same time in both events for the first phase, but delayed by 1 h for the second phase (17:00 UT for E15 and 18:00 UT for E13).

In terms of vTECrel two different phases are also discerned, centered at 12:00 UT and around 20:00 UT, respectively. The maximum peak of the first phase occurs again simultaneously on both events. On the second phase, the maximum peak, which is the largest during the day for both events, begins around 20:00 UT in E15 and around 20:30 UT in E13. The disturbance that appear only during E15 around 22:00 UT in both vTEC and vTECrel, is related to an anomaly in the processing technique due to a reduced number of satellites in view during that specific hour. In this second phase a smaller second peak, which is better seen in vTECrel, appears in both events. This peak occurs at around 22:30 UT for E13 and at around 23:30 UT for E15. After this time, both vTEC and vTECrel decrease on 18 March from 02:00 UT until around 05:00 UT and is less intense than the positive stage. The decrease is briefer and more intense in E15.

About the profile of meanROT curves, the first feature that arises is the wavelike structures from 08:00 UT to 13:00 UT on 17 March. These structures are better analyzed in Figure 3 which shows ROT values for each GPS satellite in view over MAD2 (with an elevation mask of 30°) on 17–18 March 2013 (top) and 2015 (bottom). In both events, ROT curves present simultaneous undulating structures with a parallel cadence. They appear after the onset of the geomagnetic storm and are attributable to large-scale TIDs (LSTIDs). Note in Figure 1 that until 10:00 UT on 17 March, both events show the same period and phase, and that from 10:00 UT to 13:00 UT the phase changes and the amplitude increases more in E13 than in E15. Additionally, in E15 large amplitude wavelike structures again related to LSTIDs occur from 14:00 UT to 03:00 UT of the following day, and they are especially intense from 14:00 UT to 19:00 UT. When analyzing the interval from 15:00 UT to 18:00 UT, noisier structures are modulated with the related TIDs structures, characterized by faster fluctuating ROT, and probably caused by the presence of smaller scale structures in the ionosphere. It is worth noting that the irregular structures continue on 18 March for E15 but not for E13. The changes observed in the amplitude of the wavelike structures on 17 March follow also the same pattern indicated by geomagnetic indices, and for E15 a significant ionospheric uprising in the European sector has been detected with ionosonde data (Nayak et al., 2016). The event started at 18:30 UT on 17 March, lasted almost 10 h and was accompanied by decreases in f_oF_2 at the same stations where the h_mF_2 increase was observed. These data confirm the remarkable energy level of E15 and the vTEC decrease revealed in Figure 1.

3.2. Background State of the Local Geospace Response (13–20 March)

Figure 2 shows the period starting 4 days previous to the event on 17 March up to 3 days after the event. This figure is used in this section to study the background state for the events. The panels represent the same data as in Figure 1.

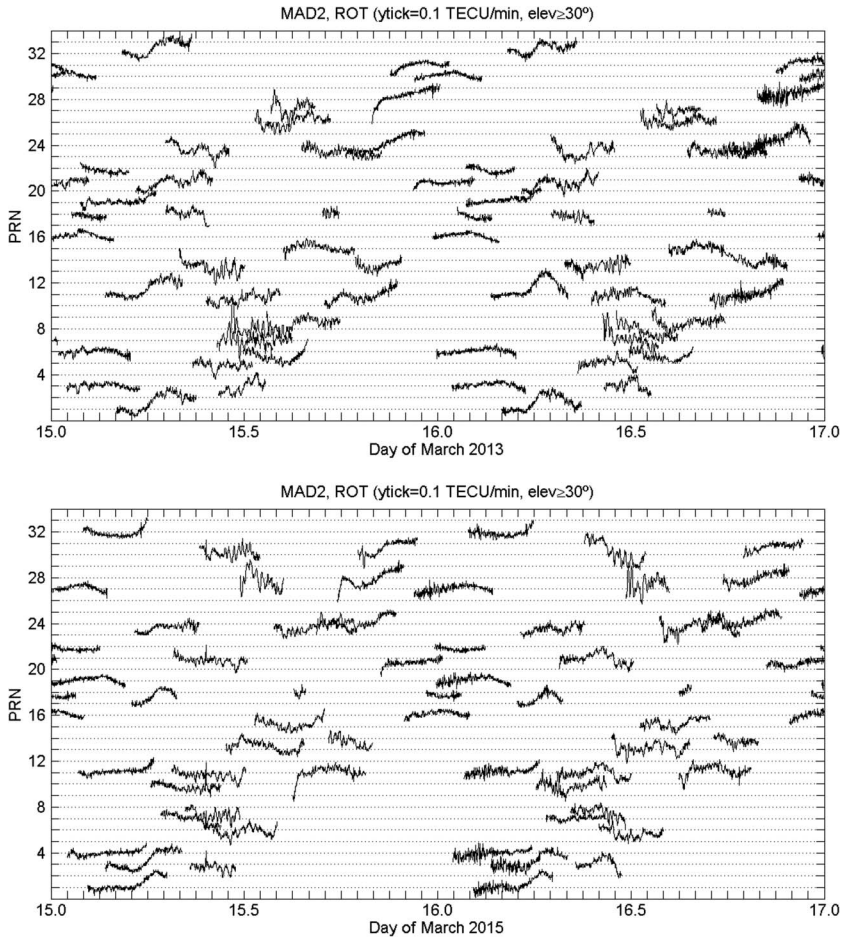

Figure 4. ROT for each GPS satellite over MAD2 station on 15 and 16 March (top) 2013 and (bottom) 2015. Satellites elevation mask: 30°.

The auroral activity, as seen by *AL* and *AU* indices, shows very similar activity before the events but considerably different behavior from 18 March onward; for E15 the activity keeps high for both indices during more than 3 days, but for E13 the activity gets atypically quiet for both indices during the next 2 days after the storm (18–19 March).

On the ionosphere there are also differences between the two cases studied. For E15, the days before 17 March are very quiet: vTEC follows the average values and vTECrel does not exceed the threshold until 17 March. However, for E13, a continuous increase on vTEC daytime values is observed day by day since 14 March. Additionally, a remarkable increase is noted in vTECrel, which exceeds 50% from 22:00 UT on 16 March to 06:00 UT on 17 March. After the large disturbances, there are also differences between both events. For E15, the decrease observed on vTECrel remains during the three following days and four significant decreases are discernible until 20 March. Meanwhile, for E13 the ionospheric disturbance ends on 18 March at 18:00 UT and the vTECrel values do not reach the threshold value after 18 March.

Regarding ROT curves, the kind of irregularities observed the days prior and after these geomagnetic storms are daytime TIDs, which in literature are referred as medium scale TIDs (MSTIDs). They present smaller amplitudes and periods than the ones observed during the main phase of the geomagnetic storm and do not have the same phase cadence in all the satellites in view (Figure 4). Additionally, a spike related to a sudden increase in TEC (SITEC) due to a solar flare is observed on 15 March 2015 at around 09:30 UT (bottom panel of Figure 4). On the other hand, it is worth mentioning the influence of the long-lasting energy input on E15 during the recovery phase of the storm in comparison with the null energy introduction by E13 especially on day 19, which is also manifested in the ROT values reached those days (see Figure 5).

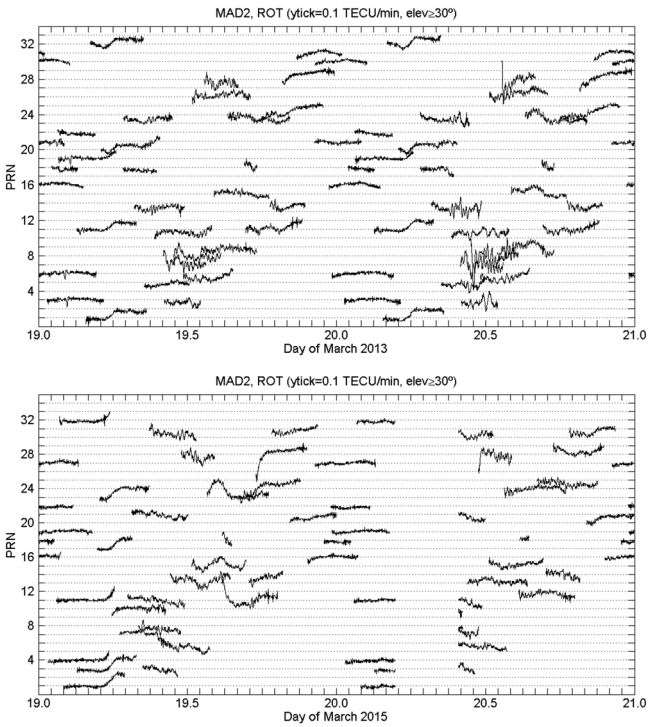

Figure 5. ROT for each GPS satellite over MAD2 station on 19 and 20 March (top) 2013 and (bottom) 2015. Satellites elevation mask: 30°. Data gap on 20 March 2015.

4. Solar and Interplanetary Geoeffective Sources

In this section we describe and analyze solar activity and interplanetary structures previous to the days of the storms. We look for geoeffective features able to explain the geomagnetic responses found on previous sections. A subsection has been dedicated to each of the events.

4.1. Solar and IP Sources for 2013 Event

Interplanetary data for 15–20 March 2013 are shown in Figure 6. Figure 6 (first panel) shows 0.31–4.80 MeV ion (mostly protons) differential intensity time profiles (color curves) and 0.175–0.315 MeV electron intensities (black curve). Figure 6 (second panel) shows interplanetary magnetic field data, indicating the magnitude (black line) and B_z component in GSM coordinates (blue line). Next panels show solar wind plasma data: solar wind speed (V_{SW}), proton temperature (T), proton density (N_p), Fe charge state composition ($< Q_{Fe} >$), Oxygen^{7+} to Oxygen^{6+} ion abundances ratio (O^{7+}/O^{6+}), thermal velocity of Helium^{2+} ion (Vth He^{2+}), and Helium^{2+} to Hydrogen^{+} ion abundances ratio (He^{2+}/H^{+}). In this last panel we show also the 0.1 threshold level with a gray dashed line as a reference.

Two forward shocks are indicated by solid lines on 15 March at 04:42 UT (S1) and 17 March at 05:27 UT (S2). These times of the shock passages agree with those detected by WIND spacecraft and reported in both the Harvard-Smithsonian Cfa Interplanetary shock Database (www.cfa.harvard.edu/shocks/) and the Heliospheric Shock Database (www.ipshocks.fi) maintained at the University of Helsinki. Data gaps are present in ACE solar wind plasma shown in the figure, which impede an accurate identification of the shocks. The first IP shock increases solar wind speed up to 450 km s^{-1}, remaining close to that value for almost 2 days. Simultaneously the O^{7+}/O^{6+} ratio is very low (less than 0.2), as corresponds to the material flowing from a coronal hole (CH), which is located in the solar disk southwest. The polarity of the CH is positive as seen by remote SDO/HMI data and consistent with in situ IMF data (Bx[GSM] <0). The second shock on 17 March at 05:27 UT is stronger, increasing the solar wind speed from less than 450 km s^{-1} to over 700 km s^{-1}. The driver of this IP shock is an interplanetary coronal mass ejection (ICME) with recognizable features about 9 h later. Between this shock and the ICME, B_z was highly fluctuating, as commonly found in sheaths. It is difficult to set the rear boundary of the ICME as some features (typically found on these structures) are found on the data but their timings do not match. For example, a smooth rotation of the magnetic field vector appears on 17 March from 14:38 UT until the end of the day; consequently, attending to magnetic topology, the ICME might be considered to be found on that interval. In contrast, an interval of decreased temperature is present from 18 March 09:50 UT to 19 March 13:55 UT and enhanced and smooth (when compared to previous solar wind) magnetic field is found until the end of 19 March, thus defining a broader range for the boundaries.

Attending to composition, enhanced helium abundances ($He^{2+}/H^{+} \geq 0.06$) typically associated with ICMEs are observed since the beginning of 18 March until noon on 19 March, being for some hours well over 0.1 after 19:00 UT on 18 March which indicates the presence of ICME material (Borrini et al., 1982). A data gap prevents the determination of the end of the enhanced helium abundance. Solar wind recovers normal values after that, at the end of 19 March. The average Fe charge state reaches values as high as 14 close to 2 UT on 19 March. The O^{7+}/O^{6+} ratio is higher than the expected values in the same interval where average Fe charge states are high. These composition anomalies indicate that the temporal interval where we find ICME material extends for more than two days from 17 March to 19 March. Considering also the complexity in magnetic field vector signatures together with the other solar wind plasma parameters, several ejections are expected to be involved in this interval.

Analyzing remote data, the CME candidates able to explain in situ interplanetary signatures are three, which are summarized in Table 1 (hereinafter, CME timings correspond to the first observation in LASCO C2). On 15 March at 07:12 UT, a full halo CME is observed with plane-of-the-sky (POS) speed of 1,000 km s^{-1}. It originates two deep coronal dimmings, one at AR 11692 and another one at an equatorial location. This event converted

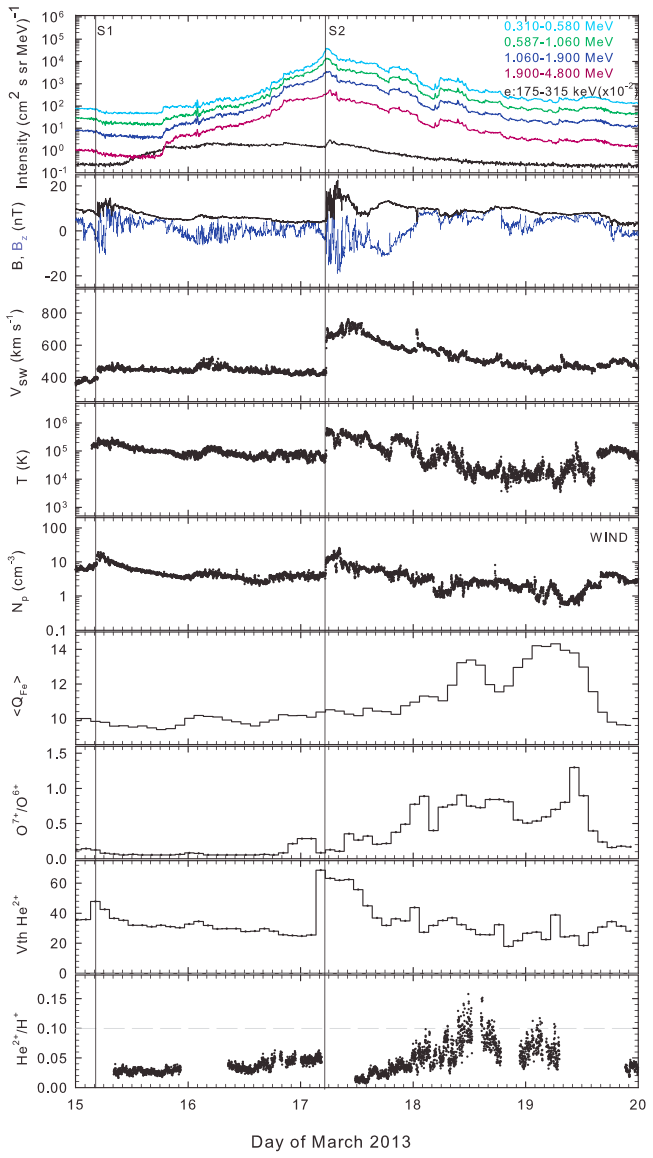

Figure 6. Interplanetary data for the period 15–19 March 2013. (first panel) The 0.31–4.80 MeV ion (mostly protons) differential intensity time profiles (color curves) and 0.175–0.315 MeV electron intensities (black curve). (second panel) The interplanetary magnetic field data, indicating the magnitude (black line) and B_z component in GSM coordinates (blue line). Next panels show solar wind plasma data: solar wind speed (V_{SW}), proton temperature (T), proton density (N_p), Fe charge state composition ($< Q_{Fe} >$), Oxygen^{7+} to Oxygen^{6+} ion abundances ratio (O^{7+}/O^{6+}), thermal velocity of Helium^{2+} ion (Vth He^{2+}), and Helium^{2+} to Hydrogen^{+} ion abundances ratio (He^{2+}/H^{+}). In this last panel we show also the 0.1 threshold level with a gray dashed line as a reference.

the previous CH with negative magnetic polarity into a larger bird-shaped CH located at the solar central meridian on 15 March. The associated ejected filament exhibited dextral chirality, in agreement with a right-handed flux rope, as observed at interplanetary medium on 17 March from 14:38 UT to midnight. This CME is related to an M1.1 X-ray flare on 15 March at 05:46 UT, emitted at N09°E06°. On 16 March another CME is detected at 06:00 UT, with POS speed of about 280 km s^{-1}, almost coincidental with a C2.7 flare and also related to a filament eruption at 05:12 UT from the south of AR 11698. However, it is difficult to assess the filament chirality. At the interplanetary medium, the IMF presents fluctuations, nontypical of ICMEs, and a flux rope structure is difficult to guess either on 18 or 19 March and, therefore, the helicity cannot be provided. Just attending magnetic field signatures, the ICME material may be unnoticed but composition anomalies indicate that it extends more than the interval of the flux rope on 17 March. This disagreement between magnetic and composition signatures may appear by merging of magnetic topologies from an eruption related to both the AR and the bird-shaped CH (i.e., Cid et al., 2016). The third CME was observed on 16 March at 14:50 UT on the SW limb with POS speed of 800 km s^{-1} and related to a large eruption from AR 11690 seen 50 min before with dextral chirality. It is not possible to discard CME material merging with the solar wind on the interval analyzed.

Solar energetic particle (SEP) data are shown in Figure 6 (first panel). For the sake of clarity, we only show the low-energy (< 4.8 MeV) proton differential intensity channels measured by ACE/EPAM, although the intensity enhancement extended in energy up to ~40 MeV protons (GOES-13/EPEAD differential channels, not shown here). The proton intensities increase from ~17 UT on 15 March until the time of the interplanetary shock passage on 17 March, when the intensity reached the peak, suggesting a central meridian origin for the main source of particles. On the other hand, the near-relativistic electrons (black curve in Figure 6, first panel) start to smoothly increase, shortly after the onset time of the Halo CME on 15 March at 07:12 UT. These two latter facts suggest that the Halo CME is the main solar source in E13. This agrees with the association reported by Wu et al. (2016) based on LASCO and STEREO (ST) observations of the shock in white light images. ST-B observed the CME eruption at 06:15 UT and ST-A at 06:25 UT. The onset of the particles occurred at about 19 UT, thus delayed about 12 h from the onset of the CME at 7 UT. This delayed onset may be caused by the disturbed solar wind conditions at 1 AU, which do not favor a direct connection of the observer (ACE, near Earth) with the shock at the beginning of the event. Note that the onset of the proton intensities is preceded by the fast solar wind from a CH that may modify the IMF from the nominal Parker Spiral and hence preventing fresh particles from the shock to arrive at ACE/Earth location. Wu et al. (2016) modeled the CME shock propagation using solar photospheric magnetograms observed on 15 March to model the input conditions for the solar wind using WSA (Wang-Sheeley-Arge) model. These authors conclude that the delayed particle onset comes from the fact that, at the onset, the CME was in another magnetic sector than the Earth, preventing the particles to reach the Earth's magnetic flux tube, until the CME shock crossed the same magnetic sector of the Earth, when the SEP enhancement is seen.

4.2. Solar and IP Sources for 2015 Event

Figure 7 shows interplanetary data for E15 using the same format as Figure 6. The solar wind speed profile from 15 to 20 March resembles that of a stream interaction. Starting from typical normal solar wind values close to 300 km s^{-1} at the beginning of 15 March, the solar wind speed slowly increases during almost 3 days until reaching values close to 600 km s^{-1}, typical of fast streams, on 18 March. Large proton temperature,

Table 1
Geoeffective CME Candidates for the Event on 2013

Day of 2013	CME detection (UT)	POS speed (km s^{-1})	Filament chirality	AR	Flare
15 March	07:12 (Halo)	1000	Dextral	11692	M1.1 (05:46)
16 March	06:00	280	Not clear	11698	C2.7
16 March	14:50	800	Dextral	11690	

low proton density, and Alfvénic fluctuations present in both solar wind velocity and magnetic field strength, fully support that the ACE spacecraft was inside a fast stream from a CH during 18–19 March. However, the value of the magnetic field strength reaching more than 30 nT on 17 March is too high when comparing to other typical interaction regions. The appearance of an interplanetary shock on 17 March at 04:00 UT, indicated by a solid line (S) in Figure 7, before the enhanced magnetic field strength is not either a common feature of interaction regions but of an ICME that drives it. A SEP event is also seen for $E < 4.8$ MeV (Figure 7, first panel), with low-energy particles peaking close to the shock passage supporting the hypothesis of an ICME-driven shock.

The average Fe charge state reaches values over 11 on 17 March between 14 UT and 20 UT. According to Lepri and Zurbuchen (2004), high Fe charge states are an excellent sufficient signature to identify ICMEs. The appearance of CME material in the interval corresponding to the interaction region is also supported by the helium to proton number density ratio. In spite of some data gaps, enhanced helium abundances, typically associated with ICMEs, are observed late on 17 March and early on 18 March, see bottom panel). Indeed, the Helium number density on the first 2 h of 18 March exceeds largely by 10% the proton number density.

When analyzing the O^{7+}/O^{6+} ratio, a step-like discontinuity appears at the time of the IP shock dropping the O^{7+}/O^{6+} ratio below 0.1 until the end of 19 March but two small intervals on 17 March when it reaches up to 0.2. On the other hand, a step-like discontinuity in the thermal velocity of He^{2+} appears about the same time when O^{7+}/O^{6+} ratio drops, and remains high until the end of the interval analyzed. A low O^{7+}/O^{6+} ratio is considered to be a very good signature of a stream from a CH (Zurbuchen et al., 2002), and the enhanced thermal velocity of He^{2+} indicates material from high-speed streams (HSS) (Burlaga et al., 1998).

Nevertheless, the O^{7+}/O^{6+} intervals with values close to 0.2 are consistent to the interval with high Fe charge states and enhanced helium abundances, and also to an interval with low proton temperature, suggesting the presence of an ICME. The interval can be roughly set between 17 March at 12 UT and 18 March at 5 UT, although the boundaries are slightly shifted depending on the signature used to set them. In any case, the above scenario suggests that on 17 March CME material and stream from the CH merged together through an interaction process resulting in a large increase in magnetic field strength.

Observing solar counterparts on LASCO and AIA data, an enlarged CH with negative polarity in the southern solar pole (extended up to the solar equator) appears as the source of the fast solar wind stream observed in the interplanetary medium. This large CH was in the solar central meridian on 14–16 March. Regarding the CME material, there are several CMEs and filament eruptions that may be good candidates to reach the Earth. They have been summarized in Table 2. On 14 March at around 10 UT a slow CME is ejected with POS speed of 150 km s^{-1} from the SW limb, and without clear filament ejections, indicating that it may been backsided. Another CME, the most probable source of the ICME observed on 17–18 March, is the halo CME seen on 15 March at 01:29 UT. This CME is associated with a filament eruption half an hour before from AR 12297, which shows sinistral chilarity. This CME is ejected with POS speed of 700 km s^{-1} and is associated to a C9.1 flare with onset at 01:15 UT from S22°W25°. Energetic particle observations also support the CME on 15 March as the solar source of the ICME material driving the IP shock.

The onset of the particles, both for electrons (black curve in Figure 7, first panel) and high-energy protons (<40 MeV in this event not shown here), is immediately after the onset of the CME/flare pair and low-energy protons (color curves) peak close to the shock passage, both facts suggesting a western origin near the central meridian for the source of particles. Particle intensities show irregular profiles up the shock detection. These intensity abrupt changes are simultaneous for all proton energies and for electrons and do follow changes

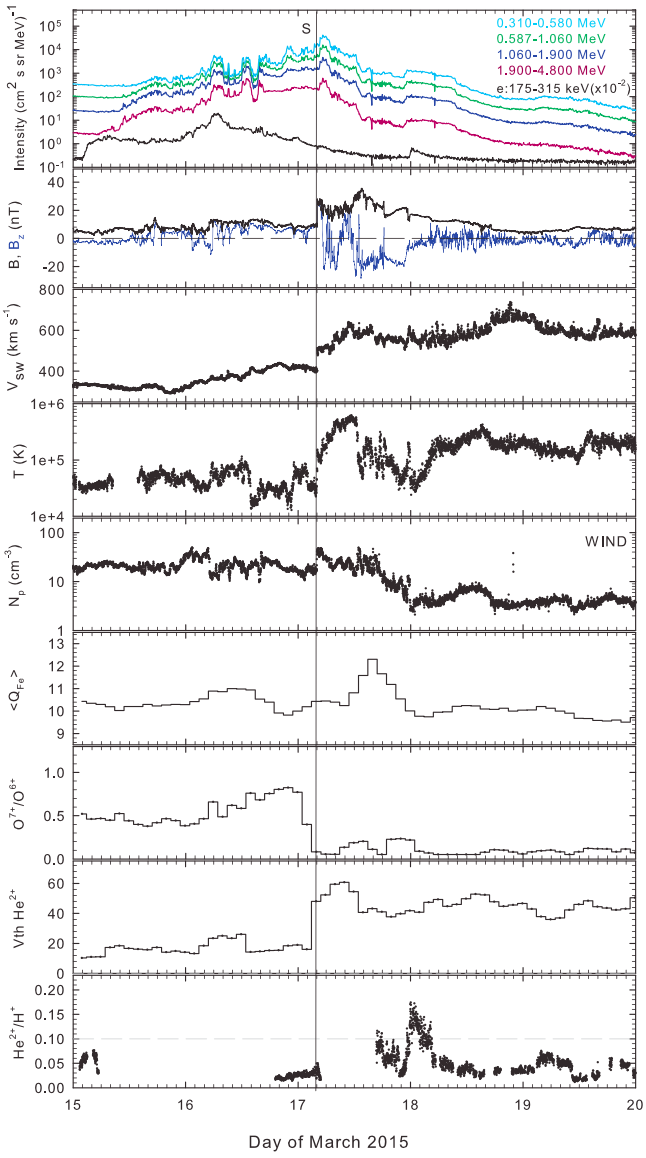

Figure 7. Interplanetary data for the period 15–19 March 2015. (first panel) The 0.31–4.80 MeV ion (mostly protons) differential intensity time profiles (color curves) and 0.175–0.315 MeV electron intensities (black curve). (second panel) The interplanetary magnetic field data, indicating the magnitude (black line) and B_z component in GSM coordinates (blue line). Next panels show solar wind plasma data: solar wind speed (V_{SW}), proton temperature (T), proton density (N_p), Fe charge state composition ($< Q_{Fe} >$), Oxygen^{7+} to Oxygen^{6+} ion abundances ratio (O^{7+}/O^{6+}), thermal velocity of Helium^{2+} ion (V_{th} He^{2+}) and Helium^{2+} to Hydrogen^{+} ion abundances ratio (He^{2+}/H^{+}). In this last panel we show also the 0.1 threshold level with a gray dashed line as a reference.

in the local IMF. After the main solar source, two other eruptions took place, M class X-ray flares on 15 March at 22:42 UT (S19°W32°) and on 16 March at 10:39 UT (S1°W39°). We cannot rule out that these eruptions contributed to the injection of new particles in the magnetic flux tubes connected to the Earth, but this seems unlikely because temporally associated CMEs are very slow for accelerating particles (POS speed <600 km s^{-1}). The third row in Table 2 corresponds to a filament eruption with sinistral chirality from the SW limb on 16 March at 16:15 UT. CME detection is not confirmed since a large LASCO data gap exists.

Figures 8a and 8b show composite images of the halo CME for E13 and E15 in SOHO/LASCO C2 images, and the corresponding SDO/AIA 193 Å image. Figures 8c and 8d show some relevant features displayed in EUV, related to the halo CMEs: for E13, a decaying flare and a dimming opening up close to the bird-shaped CH are shown in 193 A, just after the SDO eclipse. Unfortunately, the ejection onset happened during the SDO eclipse. For E15, part of the material ejected from the halo CME is visible in the SW part of AIA 304 Å image. SDO/AIA images are clipped in intensity and plot in logarithmic scale.

5. Discussion

Several similarities and differences have been found between both events in the analysis on previous sections, which have propagated similarly on all the stages of the Sun-Earth chain. They have similar interplanetary structures (CME + HSS) participating on the events, but they play different roles during their travel toward Earth, which resulted in different geoeffectiveness. The intensity of the storms differs, but they have a surprisingly similar evolution of the long and nontypical main phase as seen by both the response on the geomagnetic field and the ionosphere. Strong local disturbances, with similar profiles but again less intense during 2013 have also been found. All of these features are examined in more detail in this section using Figure 9, which collects different parameters from both events for the period 17–19 March.

5.1. Different Intensities for Similar Geomagnetic Storms

The expected response of the magnetosphere to solar wind input (ERC-H signal in section 3.1) closely follows the response observed on the ground. This means that the analysis of interplanetary signatures only is able to give an answer for the difference in intensity between both geomagnetic storms (being the intensity of E15 geomagnetic storm almost twice the intensity of E13).

The periods of negative B_z during 17 March are similar for E13 and E15 (Figure 9, third panel) as expected when analyzing the timing of development of their main phases. Thus, their different peak intensities are due to a larger energy input given by a more intense dawn-dusk convective electric field, which depends on the product of the solar wind speed and B_z component as specified in section 2.3. Solar wind speed is higher during E13, but in a small percentage compared to a more than double B_z intensity for E15, occurring mostly after 12 UT, in agreement also with the time when the intensity of the geomagnetic disturbance during the main phase of E15 starts to be larger. These primary features (similar timing of the disturbance and higher intensity for E15) during the main phase of the geomagnetic field are also followed by *SYM-H*, suggesting the presence of common features with global character. SPT-H shows similar features as the result of ring current enhancement. Ionospheric disturbances follow the same trend, showing similar timing of occurrence of the rise and fall in both events. Also, during E15 the intensity of the disturbances (both in vTEC as in vTECrel) are considerably higher than in E13.

Table 2
Geoeffective CME Candidates for the Event on 2015

Day of 2015	CME detection (UT)	POS speed (km s^{-1})	Filament chirality	AR	Flare
14 March	10:00	150	Not applicable		
15 March	01:29 (Halo)	700	Sinistral	12297	C9.1
16 March	LASCO gap	LASCO gap	Sinistral (16:15)		

5.2. CME Interactions with HSS

The cause of a stronger B_z during E15 can be found in the analysis of interplanetary sources in section 4. During E15, the ICME triggering the event is traveling ahead of a faster HSS, as shown in Figure 7; solar wind speed for E15 is increasing after the shock, which is a clear indication of compression of the ICME by the HSS, and the most probable cause of a strengthened IMF (Wu et al., 2016). For E13, the ICME arrived days after the arrival of a HSS with a speed much lower than the ICME. The speed of the solar wind behind the ICME is decelerating, which suggests an expanded ICME which may lessen the strength of the IMF B_z, as opposed to the situation in E15.

We have identified only one ICME responsible for the triggering of each geomagnetic storm; nonetheless, each of them interacted with interplanetary HSS coming from CHs. For E13 we have considered also other ejections involved during the evolution of the event. Several authors have identified more than one interplanetary structure from different ejected material from the corona, which triggered the events. In the case of E15,

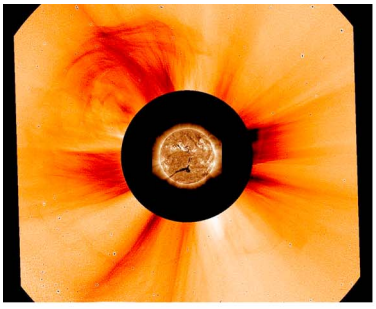

(a) Image composite of AIA 193A and LASCO C2 inverted color, on 2013 March 15 at 07:50 UT made with JHelioviewer. The main structure of the halo CME is visible in the NE part of the image.

(b) Image composite of AIA 193A and LASCO C2 inverted color, on 2015 March 15 at 02:48UT made with JHelioviewer. The main structure of the halo CME is visible in the W part of the image.

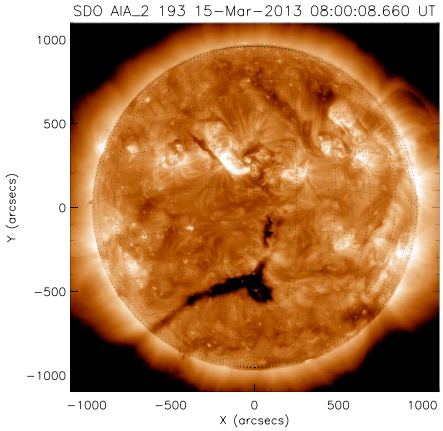

(c) SDO/AIA 193A on 2013 March 15 at 08:00 UT, just after the CME ejection. This image is taken 30 min after the end of the eclipse.

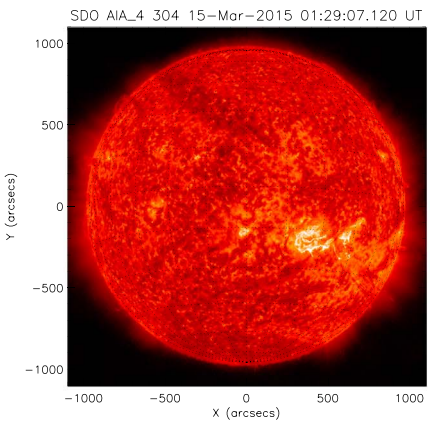

(d) SDO/AIA 304A image on 2015 March 15 at 01:29 UT, where a large amount of mass is expelled in the halo CME. Part of this mass is visible in the SW part of the panel.

Figure 8. Most relevant features of the solar sources for (a, c) E13 and (b, d) E15.

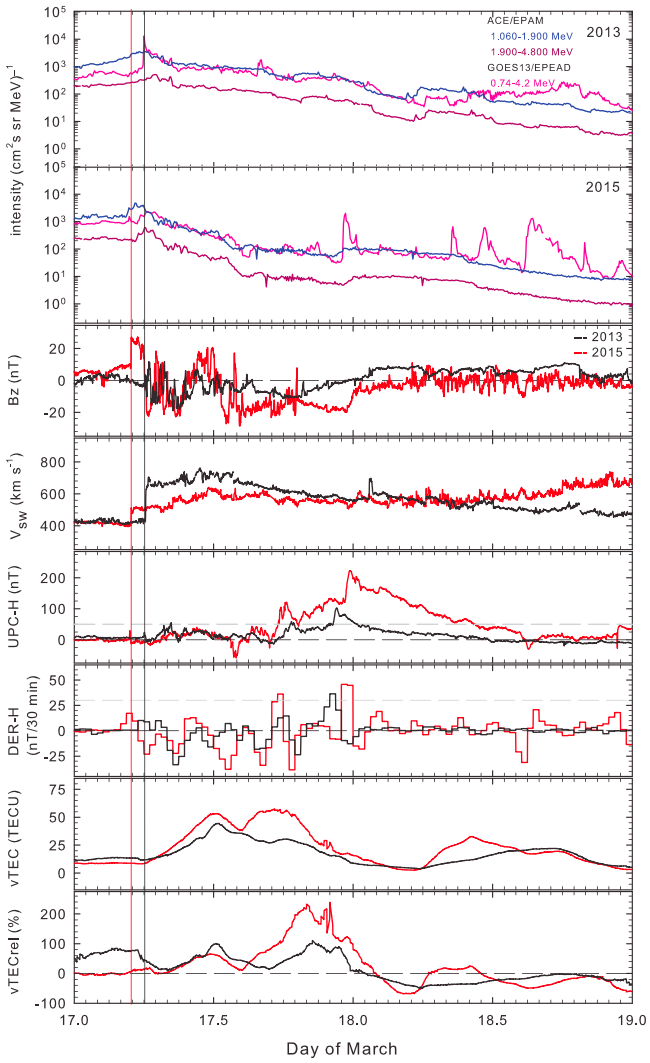

Figure 9. Interplanetary and geospace response data for E13 and E15. From top to bottom, ion (mostly protons) differential intensity time profiles of 1.06–1.90 MeV and 1.90–4.80 MeV channels of ACE/EPAM instrument (outside the magnetosphere) and the 0.74–4.20 MeV channel of GOES/EPEAD instrument (inside the magnetosphere), (first panel) for E13 and (second panel) for E15; the following two panels show (third panel) magnetic field component (B_z) in GSM coordinates, (fourth panel) solar wind speed (V_{SW}) (shifted 42 and 50 min for E13 and E15, respectively, to account for the traveling time to the Earth); next two panels show the (fifth panel) unpredicted contribution of the horizontal geomagnetic field, UPC-H and (sixth panel) the 30 min derivative of the geomagnetic field, DER-H; and the last two panels show, (seventh panel) vertical total electron content, vTEC and (eighth panel) relative variation of TEC, vTECrel.

Joshi et al. (2016) explained the two-step decrease of *Dst* index by identifying two ICMEs. The composition analysis of the interplanetary medium given in section 4 in this work does not support a second ejecta from the corona for E15 and the triggering of the geomagnetic storm is explained by the encounter and merging of the HSS and the ICME resulting in the enhancement of the IMF B_z component. The particle intensities analysis in this work also provides support for the identification of just one ICME. In the case of E13, Wu et al. (2016) identified two magnetic clouds (MCs) contributing to the geomagnetic storm. In this work we ascribe the triggering of the E13 storm to the interaction of the ejecta with the HSS, similar to E15 and although other ejecta have been identified to reach the Earth, they are not directly related to the triggering of the storm.

5.3. Strong Local Geospace Disturbances

The local character of the geospace response has been analyzed in section 3 using the signal UPC-H, which gives the difference between the geomagnetic disturbance on the ground (from measurements at SPT-H) and the theoretical expectations as measured by ERC-H. It is worth noting that ERC-H gives the expected effect of the ring current enhancement, thus having a global character, avoiding to explain different disturbances (for low/middle latitudes) at different longitudes at the same storm time. UPC-H signal shows not only deviations of the local responses from the global one, but also deviations of the expected global signal from the real one, which are part of the uncertainties. It is worth noting that it is possible to obtain an equivalent UPC-H magnitude from the deviations of SPT-H from global geomagnetic indices as *Dst* or *SYM-H*; but these indices suffer from being influenced by local disturbances because of their limited spatial resolution and location of their data sources (geomagnetic observatories). Because the analysis in section 3 focuses on the local responses, we have chosen to obtain UPC-H from ERC-H, which is not influenced by local disturbances, as it depends solely on solar wind input.

The results in section 3.1 show that both events have similar and strong positive disturbances (see UPC-H in Figure 1) especially at dusk and midnight. These are typical patterns of FACs that can be found at midlatitude which are involved in the substorm current wedge (SCW) during substorm events (Kepko et al., 2015; Meng & Akasofu, 1969). The contribution of substorms to the enhancement of the ring current has been a special topic of interest since long (He et al., 2016), which is mainly originated by the use of global indices like *SYM-H*, which are biased by other effects different from the ring current. From the results in section 3.1, these two St. Patrick events show strong influences of substorm activity on the local geomagnetic field which may have a direct effect on these global indices.

The strongest of these features occurs for E15 near midnight. This is related to the north turning of B_z IMF, which may have triggered the substorm expansion phase (McPherron et al., 1986), when a dipolarization of the geomagnetic field occurs (Lyons, 1995; Lyons et al., 1997). The intensity of these disturbances is larger for E15 than for E13, which may be the result of the strong north turning of B_z (Wei et al., 2011) due to the compression of the ICME by the HSS. This dipolarization event near midnight is also supported by the differential proton intensity channels shown in Figure 9. Several intensifications of the 0.74–4.2 MeV channel from GOES13/EPEAD occur right before midnight UT of 17 March, which are not seen on ACE/EPAM equivalent channels (outside of the magnetosphere) proving their substorm origin. Goldstein et al. (2017) also reported burstly flows of lower energy channels up to 40 keV for E15 on the same timing reported in this work.

Ionospheric data also show similar disturbances, the strongest increase of vTECrel occurs on the second phase which goes from dusk to midnight. Moreover, this second phase appears as a double peak that can be related also to effects on the ionosphere of the SCW field-aligned currents (Block & Fälthammar, 1968; Rishbeth, 1997). The second peak occurs during the periods of substorm activity.

ROT curves show the presence of LSTIDs for both events, coinciding with the ascending phase of the peaks observed in vTECrel. The LSTIDs occurring from few hours after the SSC until noon exhibit larger amplitude and period than the geomagnetically quiet time TIDs observed in March. Additionally, E15 also present noisier undulations in ROT curves characterizing LSTIDs in the late afternoon (from 15:00 UT to 19:00 UT). Larger noise indicates the presence of smaller-scale irregularities or TEC gradients.

The derivative of the geomagnetic field, DER-H, shows also strong disturbances at those timing when UPC-H signal is also stronger, indicating an association with substorm activity. The derivative of the geomagnetic field is usually a good proxy for GICs, and consequently for disruption of technology (Boteler & Pirjola, 2017; Pulkkinen et al., 2017; Trichtchenko & Boteler, 2004; Viljanen et al., 2015). This has important consequences for space weather purposes, as these local and strong changes of the geomagnetic field have occurred at midlatitude locations and are associated with substorm activity, something unusual and unexpected at these locations. Moreover, this local character does not appear in global geomagnetic indices like *Dst* or *SYM-H* which focus their attention on the global character of the ring current enhancement (Cid et al., 2015; Saiz et al., 2016).

5.4. Season Implications for Moderate Geomagnetic Storms

The effects of the inclined geomagnetic and solar axes, together with the Earth rotation and revolution may also have a role in these events and especially in the substorm-related disturbances. The semiannual variation of geomagnetic activity is well known since the beginnings of the solar-terrestrial relation studies (Bartels, 1932; Cortie, 1912; Sabine, 1852). Many works have helped to simplify the problem to three hypotheses: the "axial," the "Russell-McPherron," and the "equinoctial" hypothesis (for a review see Lockwood et al., 2016). All of them show a common feature in their pattern with a maximum during equinoxes. There is also a tendency for "great storms" to clutter during equinoxes (Crooker et al., 1992; Svalgaard et al., 2002), which may also be related, but we will not discuss it in this work.

Finch et al. (2008) considered the substorm expansion phase to be responsible for the "equinoctial" pattern, and Mursula et al. (2011) studied the pattern as followed not only by the number of substorms and their intensity but also by the substorm efficiency (the product of substorm number with substorm strength). Mursula et al. (2011) concluded that the semiannual variation is actually an annual variation that alternates between spring of one solar cycle to fall of the next one. This occurs in agreement also with the alternating annual variation of their solar wind drivers (Mursula & Zieger, 2001; Zieger & Mursula, 1998). The results shown in this paper also agree with those previous works. The effects of the SCW (especially during expansion phase) have a strong influence in both events E13 and E15. They occur during the declining phase of a solar cycle (SC 24) and in spring, during the positive polarity periods when the most "efficient" (Mursula et al., 2011) solar wind comes from the solar northern hemisphere. Moreover, the effects of the SCW on the ionospheric response (vTECrel) are also contributing to the features observed by Stankov et al. (2010).

6. Conclusions

Both St. Patrick's day storms in 2013 and 2015 show a long-lasting main phase, contrary to the fast-developed main phase of typical geomagnetic storms. They show also similar timing of the evolution of their geospace disturbances during the main phase.

Solar and interplanetary sources have been identified as the CME ejected on 15 March for both events, (2013 and 2015) with the implication of the HSS from CHs that were close to the ARs identified as the sources of the mentioned CMEs. In the case of 2013, the HSS is ahead of (west from) the ejection, in contrast with the case of 2015 which is behind of (east from) the ejection, which favors for a compression of the CME and an intensification of the geoeffectiveness.

The coincidental occurrence in the time of the season of both events, which implies similar magnetospheric configuration/orientation with respect to the Sun, seems to have played a role in the way the storm

and substorm effects have developed. The St. Patrick events 2013 and 2015 are good model examples that can help to quantify the contributions of substorms to the semiannual (or annual) variation of geomagnetic activity.

We have seen that it is possible to predict most of the global features indicated by geomagnetic indices of these storms only by near-Earth interplanetary parameters (as given by ERC-H signal), but strong local disturbances have appeared at the location of the Iberian Peninsula. Those local disturbances that are present in the dusk-to-midnight sector for both events and are attributable to the substorm current wedge (SCW) current system with a considerable increase in strength during the expansion phase. These features cannot be predicted by our current understanding of the interplanetary-magnetosphere-ionosphere coupling. A surprising result in this work is the fact that they appear with a similar pattern on both events with different intensities, being greater for E15 than for E13. Also, the timing between subsequent local unpredicted disturbances are different, being shorter for E13. These results open new challenges about the possibility to predict this type of local geospace disturbances which threats technology.

The production of hazardous GICs at the Iberian Peninsula (midlatitude) for these events have been found to be related to substorm disturbances and not directly related to the depletion on the geomagnetic field due to ring current enhancement, although these peak values of DER-H have occurred during the main phase period. The St. Patrick events warn about the role of substorm-related disturbances at midlatitude locations.

Acknowledgments
This work has been supported by the Spanish Ministerio de Economía y Competitividad (MINECO) under projects AYA2013-47735-P and AYA2016-80881-P. The work at the Universitat de Barcelona has been supported by MINECO under the project AYA2013-42614-P. The work by Antonio Guerrero has been supported by University of Alcala under the program "Ayuda Posdoctoral del Programa Propio de Vicerrectorado de Investigación y Transferencia." Marta Rodriguez Bouza thanks MINECO for her contract in the project GCL2014-62113-EXP. We acknowledge the use of publicly available data products from ACE/MAG, ACE/SWEPAM, ACE/SWICS, WIND/SWE, AIA/SDO, HMI/SDO, and LASCO/SOHO. We acknowledge data from WDC from Geomagnetism, Kyoto; also, data from SDO/AIA and SDO/HMI. We also thank Data Science Centers and Teams, and the GOES and LASCO teams. SOHO is a project of international cooperation between ESA and NASA. We thank the Virtual Solar Observatory (VSO) and Helioviewer for data acquisition and visualization, respectively. This research has made use of NASA's Astrophysics Data System. We also want to thank the International GNSS Service (IGS), for providing the GNSS. The results presented in this paper rely on the data collected at observatory San Pablo-Toledo (SPT). We thank Instituto Geográfico Nacional (Spain), for supporting its operation and INTERMAGNET for promoting high standards of magnetic observatory practice (www.intermagnet.org). Data of geomagnetic indices have been supplied by Kyoto World Data Center available at http://wdc.kugi.kyoto-u.ac.jp. This paper uses data from the Heliospheric Shock database, generated and maintained at the University of Helsinki. We acknowledge also the use of the Harvard-Smithsonian Interplanetary Shock database maintained by M. L. Stevens and J. C. Kasper.

References

Alexeev, I. I., Kalegaev, V. V., Belenkaya, E. S., Bobrovnikov, S. Y., Feldstein, Y. I., & Gromova, L. I. (2001). Dynamic model of the magnetosphere: Case study for January 9–12, 1997. *Journal of Geophysical Research*, *106*(A11), 25,683–25,693. https://doi.org/10.1029/2001JA900057

Arykov, A. A., & Maltsev, Y. P. (1993). Contribution of different sources to the field of a geomagnetic storm. *Geomagnetizm i Aeronomiya*, *33*(6), 67–74.

Asmare, Y., Kassa, T., & Nigussie, M. (2014). Validation of IRI-2012 TEC model over Ethiopia during solar minimum (2009) and solar maximum (2013) phases. *Advances in Space Research*, *53*(11), 1582–1594. https://doi.org/10.1016/j.asr.2014.02.017

Bartels, J. (1932). Terrestrial-magnetic activity and its relations to solar phenomena. *Terrestrial Magnetism and Atmospheric Electricity*, *37*(1), 1–52. https://doi.org/10.1029/TE037i001p00001

Block, L. P., & Fälthammar, C.-G. (1968). Effects of field-aligned currents on the structure of the ionosphere. *Journal of Geophysical Research*, *73*(15), 4807–4812. https://doi.org/10.1029/JA073i015p04807

Borries, C., Jakowski, N., & Wilken, V. (2009). Storm induced large scale TIDs observed in GPS derived TEC. *Annales Geophysicae*, *27*(4), 1605–1612. https://doi.org/10.5194/angeo-27-1605-2009

Borrini, G., Gosling, J. T., Bame, S. J., & Feldman, W. C. (1982). Helium abundance enhancements in the solar wind. *Journal of Geophysical Research*, *87*(A9), 7370–7378. https://doi.org/10.1029/JA087iA09p07370

Boteler, D. H., & Pirjola, R. J. (2017). Modeling geomagnetically induced currents. *Space Weather*, *15*, 258–276. https://doi.org/10.1002/2016SW001499

Brueckner, G. E., Howard, R. A., Koomen, M. J., Korendyke, C. M., Michels, D. J., Moses, J. D., … Eyles, C. J. (1995). The Large Angle Spectroscopic Coronagraph (LASCO). *Solar Physics*, *162*(1), 357–402. https://doi.org/10.1007/BF00733434

Burlaga, L., Fitzenreiter, R., Lepping, R., Ogilvie, K., Szabo, A., Lazarus, A., … Larson, D. E. (1998). A magnetic cloud containing prominence material: January 1997. *Journal of Geophysical Research*, *103*(A1), 277–285. https://doi.org/10.1029/97JA02768

Burton, R. K., McPherron, R., & Russell, C. (1975). An empirical relationship between interplanetary conditions and *Dst*. *Journal of Geophysical Research*, *80*(31), 4204–4214. https://doi.org/10.1029/JA080i031p04204

Campbell, W. (1973). The field levels near midnight at low and equatorial geomagnetic stations. *Journal of Atmospheric and Terrestrial Physics*, *35*(6), 1127–1146. https://doi.org/10.1016/0021-9169(73)90010-X

Carter, B. A., Yizengaw, E., Pradipta, R., Retterer, J. M., Groves, K., Valladares, C., … Zhang, K. (2016). Global equatorial plasma bubble occurrence during the 2015 St. Patrick's day storm. *Journal of Geophysical Research: Space Physics*, *121*, 894–905. https://doi.org/10.1002/2015JA022194

Carter, B. A., Yizengaw, E., Pradipta, R., Weygand, J. M., Piersanti, M., Pulkkinen, A., … Zhang, K. (2016). Geomagnetically induced currents around the world during the 17 March 2015 storm. *Journal of Geophysical Research: Space Physics*, *121*, 10,496–10,507. https://doi.org/10.1002/2016JA023344

Cherniak, I., Zakharenkova, I., & Redmon, R. J. (2015). Dynamics of the high-latitude ionospheric irregularities during the 17 March 2015 St. Patrick'S day storm: Ground-based GPS measurements. *Space Weather*, *13*, 585–597. https://doi.org/10.1002/2015SW001237

Cid, C., Saiz, E., Guerrero, A., Palacios, J., & Cerrato, Y. (2015). A Carrington-like geomagnetic storm observed in the 21st century. *Journal of Space Weather and Space Climate*, *5*, A16. https://doi.org/10.1051/swsc/2015017

Cid, C., Palacios, J., Saiz, E., & Guerrero, A. (2016). Redefining the boundaries of interplanetary coronal mass ejections from observations at the ecliptic plane. *The Astrophysical Journal*, *828*(1), 11. https://doi.org/10.3847/0004-637X/828/1/11

Ciraolo, L., Azpilicueta, F., Brunini, C., Meza, A., & Radicella, S. M. (2007). Calibration errors on experimental slant total electron content (TEC) determined with GPS. *Journal of Geodesy*, *81*(2), 111–120. https://doi.org/10.1007/s00190-006-0093-1

Cortie, A. L. (1912). Sun-spots and terrestrial magnetic phenomena, 1898–1911: The cause of the annual variation in magnetic disturbances. *Monthly Notices of the Royal Astronomical Society*, *73*(1), 52. https://doi.org/10.1093/mnras/73.1.52

Crooker, N. U., Cliver, E. W., & Tsurutani, B. T. (1992). The semiannual variation of great geomagnetic storms and the postshock Russell-McPherron effect preceding coronal mass ejecta. *Geophysical Research Letters*, *19*(5), 429–432. https://doi.org/10.1029/92GL00377

Dessler, A. J., & Parker, E. N. (1959). Hydromagnetic theory of geomagnetic storms. *Journal of Geophysical Research*, *64*(12), 2239–2252. https://doi.org/10.1029/JZ064i012p02239

Domingo, V., Fleck, B., & Poland, A. I. (1995). SOHO: The solar and heliospheric observatory. *Space Science Reviews*, *72*(10–2), 81–84. https://doi.org/10.1007/BF00768758

Dremukhina, L., Feldstein, Y. I., Alexeev, I., Kalegaev, V., & Greenspan, M. (1999). Structure of the magnetospheric magnetic field during magnetic storms. *Journal of Geophysical Research*, *104*(A12), 28,351–28,360. https://doi.org/10.1029/1999JA900261

Finch, I. D., Lockwood, M. L., & Rouillard, A. P. (2008). Effects of solar wind magnetosphere coupling recorded at different geomagnetic latitudes: Separation of directly-driven and storage/release systems. *Geophysical Research Letters*, *35*, L21105. https://doi.org/10.1029/2008GL035399

Foster, J. C., & Rich, F. J. (1998). Prompt midlatitude electric field effects during severe geomagnetic storms. *Journal of Geophysical Research*, *103*(A11), 26,367–26,372. https://doi.org/10.1029/97JA03057

Foster, J. C., & Rideout, W. (2005). Midlatitude TEC enhancements during the October 2003 superstorm. *Geophysical Research Letters*, *32*(L12S04). https://doi.org/10.1029/2004GL021719

Gkioulidou, M., Ukhorskiy, A. Y., Mitchell, D. G., Sotirelis, T., Mauk, B. H., & Lanzerotti, L. J. (2014). The role of small-scale ion injections in the buildup of Earth's ring current pressure: Van Allen Probes observations of the 17 March 2013 storm. *Journal of Geophysical Research: Space Physics*, *119*, 7327–7342. https://doi.org/10.1002/2014JA020096

Gloeckler, G., Cain, J., Ipavich, F., Tums, E., Bedini, P., Fisk, L., … Kallenbach, R. (1998). Investigation of the composition of solar and interstellar matter using solar wind and pickup ion measurements with SWICS and SWIMS on the ACE spacecraft. *Space Science Reviews*, *86*(1), 497–539. https://doi.org/10.1023/A:1005036131689

Gold, R., Krimigis, S., Hawkins, S., Haggerty, D., Lohr, D., Fiore, E., … Lanzerotti, L. (1998). Electron, proton, and alpha monitor on the advanced composition explorer spacecraft. *Space Science Reviews*, *86*(1), 541–562. https://doi.org/10.1023/A:1005088115759

Goldstein, J., Angelopoulos, V., De Pascuale, S., Funsten, H. O., Kurth, W. S., LLera, K., … Wygant, J. R. (2017). Cross-scale observations of the 2015 St. Patrick's day storm: THEMIS, Van Allen Probes and TWINS. *Journal of Geophysical Research: Space Physics*, *122*, 368–392. https://doi.org/10.1002/2016JA023173

Gonzalez, W. D., Joselyn, J. A., Kamide, Y., Kroehl, H. W., Rostoker, G., Tsurutani, B. T., & Vasyliunas, V. M. (1994). What is a geomagnetic storm? *Journal of Geophysical Research*, *99*(A4), 5771–5792. https://doi.org/10.1029/93JA02867

Habarulema, J. B., Katamzi, Z. T., Yizengaw, E., Yamazaki, Y., & Seemala, G. (2016). Simultaneous storm time equatorward and poleward large-scale TIDs on a global scale. *Geophysical Research Letters*, *43*, 6678–6686. https://doi.org/10.1002/2016GL069740

Hanser, F. (2011). EPS/HEPAD calibration and data handbook (Tech. Rep., GOESN-ENG-048D). Carlisle, Mass: Assurance Technology Corporation.

He, Z., Dai, L., Wang, C., Duan, S., Zhang, L., Chen, T., & Roth, I. (2016). Contributions of substorm injections to *SYM-H* depressions in the main phase of storms. *Journal of Geophysical Research: Space Physics*, *121*, 11,729–11,736. https://doi.org/10.1002/2016JA023218

Heelis, R. A. (2008). Low- and middle-latitude ionospheric dynamics associated with magnetic storms. In P. M. Kintner Jr., A. J. Coster, T. Fuller-Rowell, A. J. Mannucci, M. Mendillo, & R. Heelis (Eds.), *Midlatitude Ionospheric Dynamics and Disturbances, Geophysical Monograph Series* (Vol. 181, pp. 51–61). Washington, DC: American Geophysical Union. https://doi.org/10.1029/181GM06

Jacobsen, K. S., & Andalsvik, Y. L. (2016). Overview of the 2015 St. Patrick's day storm and its consequences for RTK and PPP positioning in Norway. *Journal of Space Weather and Space Climate*, *6*, A9. https://doi.org/10.1051/swsc/2016004

Joshi, L. M., Sripathi, S., & Singh, R. (2016). Simulation of low-latitude ionospheric response to 2015 St. Patrick's day super geomagnetic storm using ionosonde-derived PRE vertical drifts over Indian region. *Journal of Geophysical Research: Space Physics*, *121*, 2489–2502. https://doi.org/10.1002/2015JA021512

Kalegaev, V. V., & Makarenkov, E. V. (2008). Relative importance of ring and tail currents to *Dst* under extremely disturbed conditions. *Journal of Atmospheric and Solar-Terrestrial Physics*, *70*(2–4), 519–525. https://doi.org/10.1016/j.jastp.2007.08.029

Kataoka, R., Shiota, D., Kilpua, E., & Keika, K. (2015). Pileup accident hypothesis of magnetic storm on 17 March 2015. *Geophysical Research Letters*, *42*, 5155–5161. https://doi.org/10.1002/2015GL064816

Kepko, L., McPherron, R. L., Amm, O., Apatenkov, S., Baumjohann, W., Birn, J., … Sergeev, V. (2015). Substorm current wedge revisited. *Space Science Reviews*, *190*(1), 1–46. https://doi.org/10.1007/s11214-014-0124-9

Kintner, P. M., Coster, A. J., Fuller-Rowell, T., Mannucci, A. J., Mendillo, M., & Heelis, R. (2008). Midlatitude ionospheric dynamics and disturbances: Introduction. In P. M. Kintner Jr., A. J. Coster, T. Fuller-Rowell, A. J. Mannucci, M. Mendillo, & R. Heelis (Eds.), *Midlatitude Ionospheric Dynamics and Disturbances, Geophysical Monograph Series* (Vol. 181, pp. 1–7). Washington, DC: American Geophysical Union. https://doi.org/10.1029/181GM02

Lemen, J. R., Title, A. M., Akin, D. J., Boerner, P. F., Chou, C., Drake, J. F., … Waltham, N. (2012). The Atmospheric Imaging Assembly (AIA) on the Solar Dynamics Observatory (SDO). *Solar Physics*, *275*, 17–40. https://doi.org/10.1007/s11207-011-9776-8

Lepri, S. T., & Zurbuchen, T. H. (2004). Iron charge state distributions as an indicator of hot ICMEs: Possible sources and temporal and spatial variations during solar maximum. *Journal of Geophysical Research*, *109*, A01112. https://doi.org/10.1029/2003JA009954

Liemohn, M. W. (2003). Yet another caveat to using the Dessler-Parker-Sckopke relation. *Journal of Geophysical Research*, *108*, 1251. https://doi.org/10.1029/2003JA009839

Lockwood, M., Owens, M. J., Barnard, L. A., Bentley, S., Scott, C. J., & Watt, C. E. (2016). On the origins and timescales of geoeffective IMF. *Space Weather*, *14*, 406–432. https://doi.org/10.1002/2016SW001375

Lyons, L. R. (1995). A new theory for magnetospheric substorms. *Journal of Geophysical Research*, *100*(A10), 19,069–19,081. https://doi.org/10.1029/95JA01344

Lyons, L. R., Blanchard, G. T., Samson, J. C., Lepping, R. P., Yamamoto, T., & Moretto, T. (1997). Coordinated observations demonstrating external substorm triggering. *Journal of Geophysical Research*, *102*(A12), 27,039–27,051. https://doi.org/10.1029/97JA02639

Mayaud, P.-N. (1980). *Derivation, meaning, and use of geomagnetic indices*, Issue 22 of Geophysical Monograph. Washington: American Geophysical Union.

McComas, D., Bame, S., Barker, P., Feldman, W., Phillips, J., Riley, P., & Griffee, J. (1998). Solar Wind Electron Proton Alpha Monitor (SWEPAM) for the Advanced Composition Explorer. *Space Science Reviews*, *86*(1), 563–612. https://doi.org/10.1023/A:1005040232597

McPherron, R. L., Terasawa, T., & Nishida, A. (1986). Solar wind triggering of substorm expansion onset. *Journal of Geomagnetism and Geoelectricity*, *38*(11), 1089–1108. https://doi.org/10.5636/jgg.38.1089

Meng, C. I., & Akasofu, S. I. (1969). A study of polar magnetic substorms: 2. Three-dimensional current system. *Journal of Geophysical Research*, *74*(16), 4035–4053. https://doi.org/10.1029/JA074i016p04035

Mursula, K., & Zieger, B. (2001). Long-term north-south asymmetry in solar wind speed inferred from geomagnetic activity: A new type of century-scale solar oscillation? *Geophysical Research Letters*, *28*(1), 95–98. https://doi.org/10.1029/2000GL011880

Mursula, K., Tanskanen, E., & Love, J. J. (2011). Spring-fall asymmetry of substorm strength, geomagnetic activity and solar wind: Implications for semiannual variation and solar hemispheric asymmetry. *Geophysical Research Letters*, *38*, L06104. https://doi.org/10.1029/2011GL046751

Nayak, C., Tsai, L.-C., Su, S.-Y., Galkin, I. A., Tan, A. T. K., Nofri, E., & Jamjareegulgarn, P. (2016). Peculiar features of the low-latitude and midlatitude ionospheric response to the St. Patrick's day geomagnetic storm of 17 March 2015. *Journal of Geophysical Research: Space Physics*, *121*, 7941–7960. https://doi.org/10.1002/2016JA022489

Nigussie, M., Radicella, S. M., Damtie, B., Nava, B., Yizengaw, E., & Ciraolo, L. (2012). TEC ingestion into NeQuick 2 to model the East African equatorial ionosphere. *Radio Science*, *47*, RS5002. https://doi.org/10.1029/2012RS004981

Ogilvie, K. W., Chornay, D. J., Fritzenreiter, R. J., Hunsaker, F., Keller, J., Lobell, J., … Gergin, E. (1995). SWE, a comprehensive plasma instrument for the WIND spacecraft. *Space Science Reviews*, *71*(1), 55–77. https://doi.org/10.1007/BF00751326

Ohtani, S., Nosé, M., Rostoker, G., Singer, H., Lui, A. T. Y., & Nakamura, M. (2001). Storm-substorm relationship: Contribution of the tail current to *Dst*. *Journal of Geophysical Research*, *106*, 21,199–21,209. https://doi.org/10.1029/2000JA000400

Pesnell, W. D., Thompson, B. J., & Chamberlin, P. C. (2012). The solar dynamics observatory (SDO). *Solar Physics*, *275*, 3–15. https://doi.org/10.1007/s11207-011-9841-3

Piersanti, M., Cesaroni, C., Spogli, L., & Alberti, T. (2017). Does TEC react to a sudden impulse as a whole? The 2015 Saint Patrick's day storm event. *Advances in Space Research*, *60*(8), 1583–1904. https://doi.org/10.1016/j.asr.2017.01.021

Prölss, G. W. (1995). Ionospheric *F*-region storms. In H. Volland (Ed.), *Handbook of atmospheric electrodynamics* (Vol. 2, pp. 195–248). Boca Raton, FL: CRC Press.

Prölss, G. W. (2008). Ionospheric storms at mid-latitude: A short review. In P. M. Kintner Jr., A. J. Coster, T. Fuller-Rowell, A. J. Mannucci, M. Mendillo, & R. Heelis (Eds.), *Midlatitude Ionospheric Dynamics and Disturbances, Geophysical Monograph Series* (Vol. 181, pp. 9–24). Washington, DC: American Geophysical Union. https://doi.org/10.1029/181GM03

Pulkkinen, A., Bernabeu, E., Thomson, A., Viljanen, A., Pirjola, R., Boteler, D., … MacAlester, M. (2017). Geomagnetically induced currents: Science, engineering, and applications readiness. *Space Weather*, *15*, 828–856. https://doi.org/10.1002/2016SW001501

Rishbeth, H. (1997). The ionospheric *E*-layer and *F*-layer dynamos—A tutorial review. *Journal of Atmospheric and Solar-Terrestrial Physics*, *59*(15), 1873–1880. https://doi.org/10.1016/S1364-6826(97)00005-9

Sabine, E. (1852). On periodical laws discoverable in the mean effects of the larger magnetic disturbances.—No. II. *Philosophical Transactions of the Royal Society of London*, *142*, 103–124.

Saiz, E., Guerrero, A., Cid, C., Palacios, J., & Cerrato, Y. (2016). Searching for Carrington-like events and their signatures and triggers. *Journal of Space Weather and Space Climate*, *6*(A6). https://doi.org/10.1051/swsc/2016001

Schaer, S., Beutler, G., Rothacher, M., & Springer, T. A. (1996). Daily global ionosphere maps based on GPS carrier phase data routinely produced by the CODE Analysis Center. In *Proceedings of the IGS AC Workshop* (pp. 181–192). Silver Spring, MD, USA.

Scherrer, P. H., Schou, J., Bush, R. I., Kosovichev, A. G., Bogart, R. S., Hoeksema, J. T., … Tomczyk, S. (2012). The Helioseismic and Magnetic Imager (HMI) Investigation for the Solar Dynamics Observatory (SDO). *Solar Physics*, *275*, 207–227. https://doi.org/10.1007/s11207-011-9834-2

Schrijver, C. J., & Mitchell, S. D. (2013). Disturbances in the US electric grid associated with geomagnetic activity. *Journal of Space Weather and Space Climate*, *3*, A19. https://doi.org/10.1051/swsc/2013041

Singh, R., Sripathi, S., Sreekumar, S., Banola, S., Emperumal, K., Tiwari, P., & Kumar, B. S. (2015). Low-latitude ionosphere response to super geomagnetic storm of 17/18 March 2015: Results from a chain of ground-based observations over indian sector. *Journal of Geophysical Research: Space Physics*, *120*, 10,864–10,882. https://doi.org/10.1002/2015JA021509

Smith, C., L'Heureux, J., Ness, N., Acuña, M., Burlaga, L., & Scheifele, J. (1998). The ACE magnetic fields experiment. *Space Science Reviews*, *86*(1), 613–632. https://doi.org/10.1023/A:1005092216668

Stankov, S., Stegen, K., & Warnant, R. (2010). Seasonal variations of storm-time TEC at European middle latitudes. *Advances in Space Research*, *46*(10), 1318–1325. https://doi.org/10.1016/j.asr.2010.07.017

Sugiura, M. (1965). Hourly values of equatorial *Dst* for the IGY. *Annals of the International Geophysical Year*, *35*, 9–45.

Sugiura, M., Kamei, T., Berthelier, A., & Menvielle, M. (1991). *Equatorial Dst index: 1957–1986*, IAGA Bull. Saint-Maur-des-Fossess, France: ISGI Publications Office.

Sun, L., Xu, J., Wang, W., Yue, X., Yuan, W., Ning, B., … de Meneses, F. C. (2015). Mesoscale field-aligned irregularity structures (FAIs) of airglow associated with medium-scale traveling ionospheric disturbances (MSTIDs). *Journal of Geophysical Research: Space Physics*, *120*, 9839–9858. https://doi.org/10.1002/2014JA020944

Svalgaard, L., Cliver, E. W., & Ling, A. G. (2002). The semiannual variation of great geomagnetic storms. *Geophysical Research Letters*, *29*, 12–1–12–4. https://doi.org/10.1029/2001GL014145

Trichtchenko, L., & Boteler, D. (2004). Modeling geomagnetically induced currents using geomagnetic indices and data. *IEEE Transactions on Plasma Science*, *32*(4), 1459–1467. https://doi.org/10.1109/TPS.2004.830993

Tsugawa, T., Otsuka, Y., Coster, A. J., & Saito, A. (2007). Medium-scale traveling ionospheric disturbances detected with dense and wide TEC maps over North America. *Geophysical Research Letters*, *34*, L22101. https://doi.org/10.1029/2007GL031663

Tsurutani, B., Mannucci, A., Iijima, B., Abdu, M. A., Sobral, J. H. A., Gonzalez, W., … Vasyliunas, V. M. (2004). Global dayside ionospheric uplift and enhancement associated with interplanetary electric fields. *Journal of Geophysical Research*, *109*, A08302. https://doi.org/10.1029/2003JA010342

Tsyganenko, N. A., & Sitnov, M. I. (2005). Modeling the dynamics of the inner magnetosphere during strong geomagnetic storms. *Journal of Geophysical Research*, *110*, A03208. https://doi.org/10.1029/2004JA010798

Viljanen, A., Wintoft, P., & Wik, M. (2015). Regional estimation of geomagnetically induced currents based on the local magnetic or electric field. *Journal of Space Weather and Space Climate*, *5*, A24. https://doi.org/10.1051/swsc/2015022

Wautelet, G., & Warnant, R. (2014). Climatological study of ionospheric irregularities over the European mid-latitude sector with GPS. *Journal of Geodesy*, *88*(3), 223–240. https://doi.org/10.1007/s00190-013-0678-4

Wautelet, G., & Warnant, R. (2015). Origin of high-frequency TEC disturbances observed by GPS over the European mid-latitude region. *Journal of Atmospheric and Solar-Terrestrial Physics*, *133*, 67–78. https://doi.org/10.1016/j.jastp.2015.08.003

Wei, Y., Wan, W., Pu, Z., Hong, M., Zong, Q., Guo, J., … Ren, Z. (2011). The transition to overshielding after sharp and gradual interplanetary magnetic field northward turning. *Journal of Geophysical Research: Space Physics*, *116*, A01211. https://doi.org/10.1029/2010JA015985

Wu, C.-C., Liou, K., Vourlidas, A., Plunkett, S., Dryer, M., Wu, S. T., & Mewaldt, R. A. (2016). Global magnetohydrodynamic simulation of the 15 March 2013 coronal mass ejection event: Interpretation of the 30–80 MeV proton flux. *Journal of Geophysical Research: Space Physics*, *121*, 56–76. https://doi.org/10.1002/2015JA021051

Zhang, W., Zhang, D. H., & Xiao, Z. (2009). The influence of geomagnetic storms on the estimation of GPS instrumental biases. *Annales Geophysicae*, *27*(4), 1613–1623. https://doi.org/10.5194/angeo-27-1613-2009

Zieger, B., & Mursula, K. (1998). Annual variation in near-Earth solar wind speed: Evidence for persistent north-south asymmetry related to solar magnetic polarity. *Geophysical Research Letters*, *25*(6), 841–844. https://doi.org/10.1029/98GL50414

Zurbuchen, T. H., Fisk, L. A., Gloeckler, G., & von Steiger, R. (2002). The solar wind composition throughout the solar cycle: A continuum of dynamic states. *Geophysical Research Letters*, *29*, 66–1–66–4. https://doi.org/10.1029/2001GL013946